Identification of paramagnetic centers in irradiated Sn-doped silicon dioxide by first-principles

L Giacomazzi, L Martin-Samos, N Richard, D Ceresoli, A Alessi

Identification of paramagnetic centers in irradiated Sn-doped silicon dioxide by first-principles

OPEN ACCESS
IOP Publishing
Journal of Physics: Condensed Matter
J. Phys.: Condens. Matter **36** (2024) 215502 (12pp)
https://doi.org/10.1088/1361-648X/ad2a0c

Identification of paramagnetic centers in irradiated Sn-doped silicon dioxide by first-principles

L Giacomazzi[1,*], L Martin-Samos[1], N Richard[2,3], D Ceresoli[4] and A Alessi[5]

[1] CNR-IOM – Istituto Officina dei Materiali, National Research Council of Italy, c/o SISSA Via Bonomea 265, Trieste IT-34136, Italy
[2] CEA, DAM, DIF, F-91297 Arpajon, France
[3] Université Paris-Saclay, CEA, Laboratoire Matière en Conditions Extrêmes, F-91680 Bruyères-le-Châtel, France
[4] CNR-SCITEC – Istituto di Scienze e Tecnologie Chimiche "G. Natta", National Research Council of Italy, via C. Golgi 19, Milano 20133, Italy
[5] Laboratoire des Solides Irradiés (LSI), CEA/DRF/IRAMIS, CNRS, Ecole Polytechnique, Institut Polytechnique de Paris, 91120 Palaiseau, France

E-mail: giacomazzi@iom.cnr.it

Received 27 September 2023, revised 30 January 2024
Accepted for publication 16 February 2024
Published 27 February 2024

Abstract

We present a first-principles investigation of Sn paramagnetic centers in Sn-doped vitreous silica based on calculations of the electron paramagnetic resonance (EPR) parameters. The present investigation provides evidence of an extended analogy between the family of Ge paramagnetic centers in Ge-doped silica and the family of Sn paramagnetic centers in Sn-doped silica for SnO_2 concentrations below phase separation. We infer, also keeping into account the larger spin–orbit coupling of Sn atoms with respect to Ge atoms, that a peculiar and highly distorted three-fold coordinated Sn center (i.e. the Sn forward-oriented configuration) should give rise to an orthorhombic EPR signal of which we suggest a fingerprint in the EPR spectra recorded by Chiodini *et al* (2001 *Phys. Rev.* B **64** 073102). Given its structural analogy with the E'_α and Ge(2) centers, we here name it as the 'Sn(2) center'. Moreover, we show that the single trapped electron at a SnO_4 tetrahedron constitutes a paramagnetic center responsible for the orthorhombic EPR signal reported in Chiodini *et al* (1998 *Phys. Rev.* B **58** 9615), confuting the early assignment to a distorted variant of the Sn-E' center. We hence relabel the latter orthorhombic EPR signal as the 'Sn(1) center' due to its analogy to the Ge(1) center in Ge-doped silica.

Supplementary material for this article is available online

Keywords: EPR, silica, Sn-E' centers, DFT, Ge-E' centers

* Author to whom any correspondence should be addressed.

1. Introduction

Ion implantation is a largely exploited experimental way to introduce point defects in a solid matrix so to functionalize the host material [1]. For instance, Sn implantation of silica constitutes a way to make silica glass a luminescent material that can be interesting for optoelectronic or even photonic applications [2–4]. Moreover, Sn-doped silica glass has recently been proved to work as a dosimetric material based on the photoluminescence of Sn point defects [5]. Incidentally we also mention that Sn related point defects have also been found [6] in irradiated, and thermally treated, nanostructured tin-silicate glass ceramics which nowadays is a very active research field [7, 8].

About two decades ago, it was remarked that Sn-doped silica based fibers exhibit extremely high photosensitivity when exposed to UV light such as the 248 nm KrF excimer laser [9, 10]. Such photosensitivity stems from the presence of optically active point defects [11–13]. In particular, absorption bands at about 4.5 eV, 4.9 eV, and 5.9 eV have been attributed to the occurrence of Sn color centers in silica [14–16] of which the band at 4.9 eV is universally attributed to the occurrence of twofold Sn centers, alternatively known as tin oxygen deficient centers (Sn-ODC) of the second type, shortly Sn-ODC(II) [17–19]. As for the Sn-ODC of the first type, i.e. the Sn-ODC(I), its structure should consist in a ≡Sn−Si≡ dimer. Yet there is no evidence concerning the optical absorption fingerprint neither of Sn-ODC(I) nor of Ge-ODC(I) centers [20, 21]. Similarly to the 5.1 eV absorption band in Ge-doped glass [22], the 4.9 eV absorption band of Sn-doped silica is bleached under UV radiation together with a concomitant increase of absorption bands at about 4.5 eV and 5.5 eV [10, 15].

Besides the 4.9 eV absorption band, twofold Sn centers in silica glass, and in other glasses, are responsible for singlet-singlet and triplet-singlet emissions at ∼4.2 eV and ∼3.1 eV which currently make them interesting for luminescence applications [3, 5, 23–27]. Yet, it is not so clear what kind of paramagnetic centers could be generated in irradiated Sn-doped silica containing twofold Sn centers [28]. In the experimental study of [11] two variants of Sn-related paramagnetic centers were identified, an orthorhombic one with $g_1 = 1.994$, $g_2 = 1.986$, and $g_3 = 1.975$, and an axial one with $g_{\parallel} = 1.994$ and $g_{\perp} = 1.977$. These centers show a huge hyperfine coupling constant (434 mT) as also observed for Sn centers in other compounds [29]. Chiodini *et al* [11] proposed an identification of these two kind of paramagnetic centers with Sn-E' centers consisting of unpaired spins in sp^3 orbitals of three-fold coordinated Sn sites, eventually decorated with a varying number of next nearest neighbors Sn atoms. By contrast, Nakanishi *et al* [15] by investigating the absorption of point defects in irradiated Ge-Sn-SiO_2 glass have shown that two distinct kinds of paramagnetic centers, Sn-E' and $(Sn^{4+})^-$ centers, are induced by the irradiation. The absorption band of the Sn-E' is indicated to be ∼6 eV, similarly to Ge-E' centers [30], while the absorption band of the $(Sn^{4+})^-$ center is located at about ∼4.4 and ∼5.4 eV, suggesting an analogy with the Ge electron center that features absorption bands at ∼4.5 and ∼5.8 eV [15, 22] and thus supporting a non Sn-E' origin for the orthorhombic signal of [11]. The model that was originally proposed for the $(Sn^{4+})^-$ center by Kawazoe *et al* consists in an electron trapped at an octahedral Sn site [31] in analogy with Sn coordination in SnO_2 crystal. The spin-density thought for the $(Sn^{4+})^-$ center has a rather spherical symmetry reflecting the high *s*-character of the center analysed in [31] and is not consistent with an orthorhombic center as the one found by Chiodini *et al* [11]. Moreover a model based on octahedral coordination does not seem very suitable for Sn point defects in silica at very low Sn-doping levels (⩽0.4 mol%) that were considered in [11, 16], thus further prompting for a dedicated theoretical investigation of Sn paramagnetic centers in silica.

First-principles electron paramagnetic resonance (EPR) calculations, e.g. based on the linear response approach of [32], have become a standard tool in many computational investigations of point defects in solids and have allowed for safely grounded interpretation of experimental data leading to the formulation of new models such as in the case of the E'_{α} and Ge(2) centers in silica [33, 34]. Concerning Sn-related paramagnetic centers in silica, as far as we know, only the so-called H(III) centers, i.e. paramagnetic hydrogenated twofold Sn centers (=$\dot{\text{S}}$n − H), have been studied by means of a first-principles approach [35]. In this work, we present a first-principles investigation of the EPR parameters of Sn paramagnetic centers (with spin $S = 1/2$) in vitreous silica (v-SiO_2) aiming at identifying the origin of the orthorhombic EPR signal reported in [11]. We deduce, by analysing our g-values distributions obtained for a large set of defect configurations, that the orthorhombic EPR signal [11] arises from a single trapped electron (STE) center at a SnO_4 tetrahedron, which is an analogue of the Ge(1) center [36], and hence we here name it 'Sn(1) center'. In such a configuration, the unpaired spin is localized at a distorted SnO_4 tetrahedron. On the basis of our calculations we also suggest that Sn forward-oriented (Sn-FO) configurations should give rise to a paramagnetic center, here named 'Sn(2) center', where the unpaired spin is localized at a three-fold Sn atom featuring a weak long bond with a three-fold O atom, of which a fingerprint may be discernible in the EPR spectra published in [11, 37, 38]. The Sn-FO may alternatively be thought as a structure obtained through the relaxation of an ionized twofold Sn atom [33]. We thus establish that not only are Sn-E' centers the analogue of E'_{γ} (i.e. Si-E') and Ge-E' centers in silica, but also that the orthorhombic EPR signal [11], i.e. the Sn(1) center, has to be considered as the Sn counterpart of the Ge(1) center in silica [33], and is not due to a variant of the Sn-E' center as supposed in [11]. Furthermore the present investigation bring a strong support in favor of an extended structural analogy between paramagnetic centers along the isoelectronic series in pure silica, in Ge-doped silica and Sn-doped silica [15, 17, 33].

2. Theoretical methodology and modeling details

The calculations carried out in this work are based on density functional theory. The Perdew–Burke–Ernzerhof exchange-correlation functional has been adopted [39]. Norm-conserving Trouiller-Martins pseudopotentials with gauge including projector augmented wave (GIPAW) reconstruction are used [40, 41] and the Kohn–Sham wavefunctions are expanded in a basis of plane waves up to a cutoff energy of 80 Ry. The Γ point was used for sampling the Brillouin zone [42]. Geometry optimizations and EPR parameters have been obtained by means of spin-polarized calculations as implemented in the QUANTUM-ESPRESSO (QE) package [43, 44]. The EPR parameters are calculated by exploiting the GIPAW method as available in the QE package [32]. Tin isotropic hyperfine couplings (Fermi contacts) are obtained by including a scalar relativistic correction [45–47], while core-relaxation effects are not considered, as they bring just a minor correction of ∼2%. Hyperfine calculations have been carried out by using for the nuclear g-factors the values given for stable isotopes as reported in [48] (in particular, for ^{119}Sn we used $g_N = -2.09456$). Actually tin in nature is found in several stable isotopes of which those carrying a 1/2 nuclear spin are ^{115}Sn with 0.34% natural abundance, ^{117}Sn with 7.68% natural abundance, and ^{119}Sn with 8.59% natural abundance. Yet, as the nuclear g-factors for ^{117}Sn (−2.002 08) and ^{119}Sn (−2.094 56) are quite close, and concentration of ^{115}Sn is negligeable, in this paper we report Fermi contacts results based on the ^{119}Sn only. In fact the average Fermi contacts obtained with all isotopes according to the natural abundance will only show minor differences (e.g. ∼2% in the case of Sn-E' centers) with respect to results assuming the occurrence of ^{119}Sn isotope only.

Preliminary g-tensor test calculations have been carried out on the free radical SnH_3 for which we calculate a $\Delta g_\perp = g_\perp - g_e = 46\,780$ ppm, that overestimates, by ∼9.6%, the DFT result of [49] based on the gauge-including atomic orbitals approach, and is in excellent agreement with the ZORA result (47 031 ppm) obtained in [50]. In the presence of such considerably large deviations of g principal values from the free electron value g_e, [51] may suggest that the non-perturbative 'converse' approach [52, 53] could show an improved convergence over system size with respect to linear response based methods. Thus we here have run several tests calculations for selected Sn-E' and STE configurations, and found that the g principal values obtained through the linear response approach [32] overestimate by a shift of ∼1000 ppm the g-values obtained with the non-perturbative approach [52] (see table S1 in the supplementary data file). The latter shifts, which may roughly correspond to the finite size effect on the g-tensor, however only weakly affect the relative differences $g_{12} = g_1 - g_2$ and $g_{13} = g_1 - g_3$ here employed for the identification of the defects. In fact g_{12} and g_{13} are identical between the two approaches [32, 52] within ∼3%. Yet, [49] points out that for a correct treatment of spin systems involving high atomic numbers [54–56], higher orders in the spin–orbital splitting should be included instead of up to first order in the magnetic field. For the latter reason we may expect both methods [32, 52] to present sizeable (a few ppt) deviations for the g-tensor of $S = 1/2$ spin system involving an atomic species with a rather large atomic number such as tin. Other sources of systematic errors in the calculation of the g_i values (up to ∼2000 ppm) and hyperfine constant (few percent) of the tin EPR centers under investigation may come from the choice of the DFT flavour and pseudopotential generation details, e.g. inclusion in valence of semicores states (see table S2 in the supplementary data file). Moreover, for the smallest supercell size used in this work, minor size effects on the hyperfine couplings and g-tensor principal values are assessed to be up to ∼4% and ∼1000 ppm (see tables S3, S4 and figures S1, S2 in the supplementary data file). However we estimate that the full analysis of the the systematic errors mentioned here above is beyond the scope of the present paper.

The two periodic Sn-doped silica supercells used in this work contain 108 atoms and 144 atoms at the experimental density (2.2 g cm^{-3}) and are hereafter referred to as model I and model II, respectively. The original silica model I and model II were previously employed to investigate silicon oxygen deficient centers (Si-ODC) in v-SiO_2 [34, 57, 58] and later used in [33] for the discussion of Ge paramagnetic centers in Ge-doped silica. On one side the chosen models allow us to carry out test comparisons along the isoelectronic series Si, Ge, Sn for the very same configurations, on the other side by using two models we can considerably increase the number (statistics) of forward-oriented and STE configurations with respect to those analysed in [33, 58].

In particular, we generated Sn-ODC configurations of the Sn-E' kind by replacing silicon atom (or germanium atom) with tin for the silicon (or germanium) three-fold coordinated site carrying the unpaired spin in ODC configurations of previous investigations [33, 58]. In this way we obtained more than hundred Sn-E' (puckered and unpuckered [58]) configurations and about twenty Sn-FO configurations. Moreover, to generate tin STEs in model I and model II, as starting configuration we took the LDA ground states of [59] and [60, 61], respectively. By replacing each Si with a Sn atom and by adding an electron to the system we obtain, after a first-principles relaxation of the structure, a tin STE configuration, so that in total we generated 84 tin STE configurations in these models [62]. We relaxed the structure of each configuration using the Broyden–Fletcher–Goldfarb–Shanno algorithm [43]. A force threshold of 0.0005 Ryd/bohr has been adopted. Tests carried out on Sn-E' configurations using a variable cell relaxation scheme to relax the simulation cell lead just to minor changes on g values (e.g. for g_{12} and g_{13} we register variations of ∼5%) not affecting the conclusions of the present work. We have also carried out EPR parameters calculations for a few positively charged Sn–Si dimer configurations, obtained as explained here above from Si–Si dimer [i.e. Si-ODC(I)] configurations of [20, 58]), which show $A_{iso}(^{119}\text{Sn}) \leqslant 100$ mT, thus indicating that Sn–Si dimers are not relevant for the discussion of the Sn-E' variants of [11, 37].

Table 1. Geometrical parameters (Sn–O, Sn–H and O–Sn–O angle) and absolute values of A_{iso}(H), $A_{iso}(^{119}Sn)$ hyperfine couplings of H(III) paramagnetic centers as calculated in this work (TW) and as obtained in [35] by using DFT-B3LYP for the atomic cluster $[(H_3SiO)_2$ Sn–H]. We also report the experimental hyperfine splitting given in [17] for H(III) centers. Standard deviations are given in parenthesis.

	Sn–O (Å)	Sn–H (Å)	O–Sn–O (°)	$\lvert A_{iso}(H)\rvert$ (mT)	$\lvert A_{iso}(^{119}Sn)\rvert$ (mT)
TW	2.02(2)	1.77(0.2)	98.9(6.7)	15.4(2.8)	301.8(17.7)
DFT-B3LYP [35]	1.95	1.79	94	14.7	—
EXPT. [17]	—	—	—	15.0	—

3. Results

3.1. EPR parameters of H(III) centers

As far as we know, Sn-related paramagnetic defects e.g. Sn-E' centers in silica have not been theoretically studied (in particular not using large periodic supercells) apart from [35] where twofold Sn and H(III) centers [17] were investigated using DFT/HF based calculations on the atomic cluster $[(H_3SiO)_2$ Sn–H]. In particular, the H(III) centers were attributed to the occurence of Sn atoms coordinated by two oxygens and a hydrogen atom [35, 63]. In this work, prior to the study of Sn-E' centers, we investigate H(III) centers as a preliminary study for which comparisons can be carried out with both experiments and previous theoretical calculations [17, 35]. Using the twofold Ge/H(II) configurations discussed in [34] we could generate H(III) configurations in the silica model I, after replacing Ge with Sn atom as mentioned hereabove in the methods section.

Concerning the geometrical parameters of the ground state of H(III) paramagnetic centers, in [35], the all electron DFT-B3LYP results indicate a Sn–O bond length of 1.95 Å , close to the one reported for the twofold Sn atom ∼1.9 Å [35], while the Sn–H length is 1.79 Å and with a O–Sn–O angle of 94°. The hyperfine coupling constant A_{iso}(H) calculated at DFT-B3LYP level in [35] is 14.7 mT, close to the experimental value of [17] of 15.0 mT. In table 1 we show the results of our calculations for H(III) centers and compare them to [35] and [17]. In our calculation the Sn–O bond length is slightly (∼3%) longer (i.e. 2.02 Å), while the Sn–H bond length is slightly (∼1%) shorter than in [35], whereas the O-Sn-O angle is sensibly wider (∼5%) than given in [35] . The average A_{iso}(H) calculated for our H(III) configurations (15.4 mT) is in fair agreement with the experimental findings (15.0 mT) of [17] and the cluster calculations of [35], thus supporting our DFT setup for the investigation of the Sn-E' centers that is discussed in the next sections. Furthermore, the calculated hyperfine coupling constant, $A_{iso}(^{119}Sn)$, although it is quite large (∼300 mT), consistently with ESR data of tin-centered radicals [64, 65] which show very large isotropic hyperfine splitting constants (∼200 mT), it is considerably smaller than reported by Chiodini *et al* [11, 16], thus further ruling out the possible occurrence of H(III) centers in those experiments. At variance, the average g principal values we calculate for our H(III) configurations, $g_1 = 2.0029$, $g_2 = 1.9932$, $g_3 = 1.9774$, correspond to $g_{12} = 0.0096$ and $g_{13} = 0.0255$ values which are not so different from those calculated for the STE and Sn-E' centers (see next section), and thus would not allow, when no other information on the hyperfine coupling constants was provided, to exclude the presence of H(III) centers in the experiments of [11, 16].

3.2. Structural properties of the Sn-E′-like and Sn-FO configurations

In Sn-doped v-SiO_2, the Sn–O bond length in the Sn-E'-like configurations is found to be on average ∼2.00 Å with a standard deviation (std) of 0.02 Å, sligthly shorter than the experimental estimate of ∼2.05–2.09 Å in rutile SnO_2 [66, 67] which features edge and corner-sharing SnO_6 octahedra. Bond angles O–Sn–O are slightly narrower (∼102°) than reported for Ge-E' in silica [33].

As compared to the case of the Si–FO [58, 68], the structure of the Sn–FO configurations is quite strained and at first sight considerably more similar to the one of a twofold coordinated Si/Ge atom [33]. The difference between Si–FO and Sn–FO structures is especially evident when looking to the $O^{[3]}$–Sn and $O^{[3]}$–Si bond distances formed by the three-fold coordinated oxygen ($O^{[3]}$): in the Sn–FO structure, the latter $O^{[3]}$-Si distances are slightly longer (∼1.75 Å) than usual Si–O bond in silica (1.6 Å), while the former $O^{[3]}$–Sn distance is remarkably longer (∼2.3 Å). By contrast for the Si–FO structure all the $O^{[3]}$–Si bond distances are ∼1.8 Å [58]. The two normal Sn-O bonds of the Sn-FO have a bond length of 1.98 (0.03) Å, while the bond between the three-fold Sn and the three-fold O is remarkably longer (∼15%) (figure 1(a)). The spreading of the latter bond is double (0.06 Å) than it was found (0.03 Å) for the corresponding bond in Si–FO configurations in pure silica [58], thus suggesting an increased structural disorder of the Sn–FO configurations. The average O–Sn–O angle in Sn–FO configurations is about 97.6°, considerably smaller than the value associated with sp^3 hybridization (i.e. 109.47°). More specifically, in these configurations, the lowest O–Sn–O angle is about 87.4° with a standard deviation of 6.6°. The largest O–Sn–O angle (between the two normal Sn–O bonds) and the last one are on average ∼106.9° and 98.4° with standard deviations of ∼6.9° and 7.8°, respectively.

The spin-density of the Sn-E'-like configuration is mainly localized on the three-fold Sn atom, and, to a minor extent, equally shared among the three oxygen nearest neighbors (figure 1(a)), consistently with the typical shape of the spin-density in Si-E' and Ge-E' centers in v-SiO_2 [33, 58, 69]. At variance for the Sn–FO configuration, the sharing of spin density is different among the three oxygen nearest neighbors (figure 1(b)), and it is indicative of an orthorhombic center.

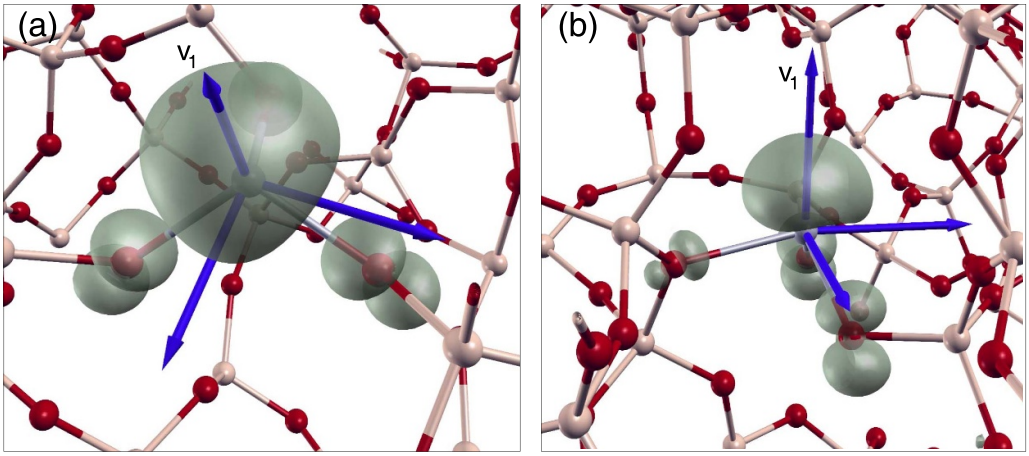

Figure 1. Ball and stick models [70] and spin densities (shadowed) of (a) a Sn-E' configuration, and of (b) a Sn forward-oriented (Sn-FO) configuration. O atoms (red), Si atoms (light brown) and Sn atom (light grey) are shown. Principal directions of the g-tensor are shown with blue arrows. For plotting the spin density a isovalue corresponding to 5% of grid maximum was used. Approximatively, the local symmetry (rotation) axis of the threefold coordinated Sn center provides the principal direction (v_1) relative to $g_1 \sim g_e$ in table 2.

Table 2. Configuration type, calculated average g principal values and Fermi contacts $|A_{\rm iso}(^{119}{\rm Sn})|$ (in mT) of Sn–FO, STE and Sn-E'-like configurations in Sn-doped v-SiO_2 compared to available experimental data ([11, 24, 37]). Standard deviations are given in parenthesis. ($g_{12} = g_1 - g_2$ and $g_{13} = g_1 - g_3$).

	References	g_1	g_2	g_3	g_{12}	g_{13}	$\lvert A_{\rm iso}(^{119}{\rm Sn})\rvert$
Sn-FO	(This work)	2.0043(11)	1.9986(31)	1.9649(57)	0.0057(25)	0.0394(59)	432(59)
STE	(This work)	2.0028(8)	1.9961(22)	1.9843(36)	0.0067(25)	0.0186(31)	480(40)
Sn-E'-ortho	(Expt. [37])	1.998	1.987	1.975	0.0110	0.0230	
Sn-E'-ortho	(Expt. [11])	1.994	1.986	1.975	0.0080	0.0190	
Sn-E'-like	(This work)	2.0035(5)	1.9892(29)	1.9810(37)	0.0144(28)	0.0225(37)	413(45)
Sn-E'-axial	(Expt. [37])	1.998	1.976	1.976	0.0220	0.0220	—
Sn-E'-axial	(Expt. [11])	1.994	1.977	1.977	0.0170	0.0170	434
Sn-E'	(Expt. [24])	1.9982	1.9836	1.9794	0.0146	0.0188	—

3.3. EPR parameters of the Sn-E′-like and Sn–FO configurations

In table 2 we show the results of the ^{119}Sn Fermi contact [$A_{\rm iso}(^{119}{\rm Sn})$] and g-tensor calculations of Sn-E'-like and Sn–FO configurations in model I and II of Sn-doped silica. The Sn-E'-like configurations (figure 1(a)) give rise to broad distributions of g_i values (figure S2 in the supplementary data file) whose averages are compared in table 2 to the experimental data reported for the Sn-E' (axial) center in Sn-doped silica [11, 24, 37]. At variance with [11, 37], our results indicate for the Sn-E' center a slight orthorhombicity (near axiality), analogously to the one previously observed for the Ge-E' centers in Ge-doped silica glass [71] and quartz [72]. The average g_1, g_2, and g_3 values suffer of some overestimation of ∼5000 to ∼10 000 ppm with respect to the experimental estimates. Incidentally we note that these overestimations exhibit a tendency to increase along the isolectronic series of Si-E' [58], Ge-E' [33] and Sn-E' centers. Considerably large (∼1000 to ∼10 000 ppm) overestimations of g_i principal values have also been reported for calculations of other $S = 1/2$ centers in wide bandgap oxides/nitrides involving atomic species of the fourth and fifth rows of the periodic table [73, 74]. The overestimation errors on g_i however tend to cancel out when considering g_{12} and, above all, g_{13} values for which we find a good agreement with the most recent experiment [24] and still a fair agreement with the axial Sn-E' of [11]. The calculated $A_{\rm iso}(^{119}{\rm Sn})$ of Sn-E'-like configurations on average underestimates only by ∼5% (21 mT) the huge experimental value of 434 mT given in [11] (table 2). The dipolar (anisotropic terms) for Sn-E' centers are quite small ($|\boldsymbol{A}_{\rm dip}|/A_{\rm iso}$ ∼6%) as compared to the isotropic (Fermi contact) term, as typical of E' centers in silica [58].

In figures 2(a) and (b) for each Sn-E' and Sn-FO configuration we show the $A_{\rm iso}(^{119}{\rm Sn})$ plotted versus g_{12} and g_{13} values. The plots, as previously found for Ge-doped silica [33], reveal the existence of two distributions of EPR parameters, the first one pertaining to the Sn dangling bond as found e.g. in puckered configurations [58], and quite well corresponding to the axial Sn-E' center [11]. A second distribution

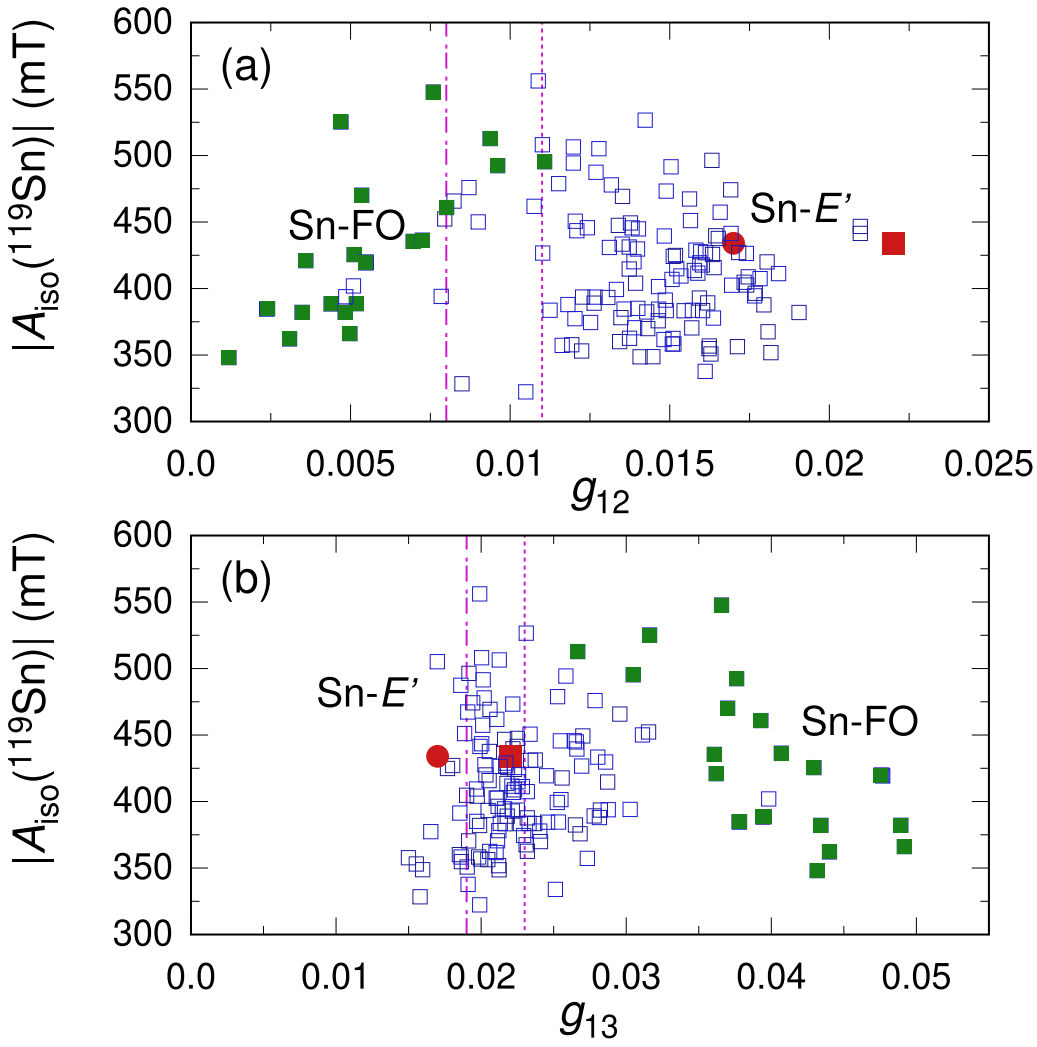

Figure 2. Calculated $|A_{iso}(^{119}Sn)|$ Fermi contacts of Sn-E'-like (blue squares) and Sn–FO (green filled squares) configurations in our models I and II plotted vs (a) $g_{12} = g_1 - g_2$ and (b) $g_{13} = g_1 - g_3$ where g_i are the g tensor principal values. Experimental data for the orthorhombic EPR signal (vertical dot-dashed line [11] and dotted line [37]) and axial EPR signal (red disc [11], red filled square [37]) are shown.

with markedly different average g_{12} and g_{13} values (table 2) arises from Sn–FO configurations. Both distributions show large variations in the hyperfine couplings: $A_{iso}(^{119}Sn)$ varies from ∼320 to ∼550 mT. The spreads of the distributions shown in figures 2 reflect the different local bonding environment experienced by each configuration [33, 58].

In analogy with the case of Ge-doped silica [33], figures 2(a) and (b) strongly suggest that Sn-E'-like and Sn-FO configurations should give rise to two well distinct EPR signals. In particular, the Sn–FO configurations should manifest themselves with a not-yet identified EPR signal hereafter named as the Sn(2) center. Moreover, figure 2 indicates that the orthorhombic signal of [11, 37] can not be attributed to Sn–FO configurations. In fact, for the latter, g_{13}^{Sn-FO} is about twice the one of the orthorhombic EPR signals of [11, 37]. Furthermore for the vast majority of our Sn-E'-like configurations, the calculated $g_{12}^{Sn-E'}$ is ∼30%–50% larger than reported for the orthorhombic Sn-E' variant [11, 37], thus making a Sn-E' center (figure 1(a)) a not so likely explanation of the orthorhombic signal [11, 37]. In addition, we have also checked the hypothetical origin of the orthorhombic signal as due to the distortions arising when other Sn atoms are included in the second nearest neighbors shell of the central threefold Sn atom [11]. In fact we have calculated the g-tensor for a representative Sn-E' configuration where we considered a varying number (i.e. zero, one and two) of Sn next-nearest neighbors of the central threefold Sn atom. Upon replacing a Si next-nearest neighbor with a Sn atom, Sn–O bonds of the Sn-E' center are uniformly elongated by ∼0.01 Å while the average O–Sn–O angle only slightly decreases by ∼1°. Upon a second Si with Sn replacement we register again similar variations with a final average Sn-O of ∼2.02 Å and O–Sn–O angle of 101.1°. As shown in table 3, the symmetry of the g-tensor is only weakly affected by the amount of Sn neighbors atoms. In particular both g_{12} and g_{13} are always larger than ∼0.0162 which undermines the interpretation of the orthorhombic Sn-E' as due to the varying number of Sn next-nearest neighbors of a threefold Sn center (figure 1(a)).

Table 3. Calculated g principal values for a representative Sn-E'-like configuration in model I where we considered a varying number of Sn next-nearest neighbors (NN^{Sn}) of the central threefold Sn atom.

NN^{Sn}	g_1	g_2	g_3	g_{12}	g_{13}
0	2.0033	1.9871	1.9788	0.0162	0.0245
1	2.0042	1.9872	1.9828	0.0170	0.0214
2	2.0049	1.9883	1.9822	0.0166	0.0227

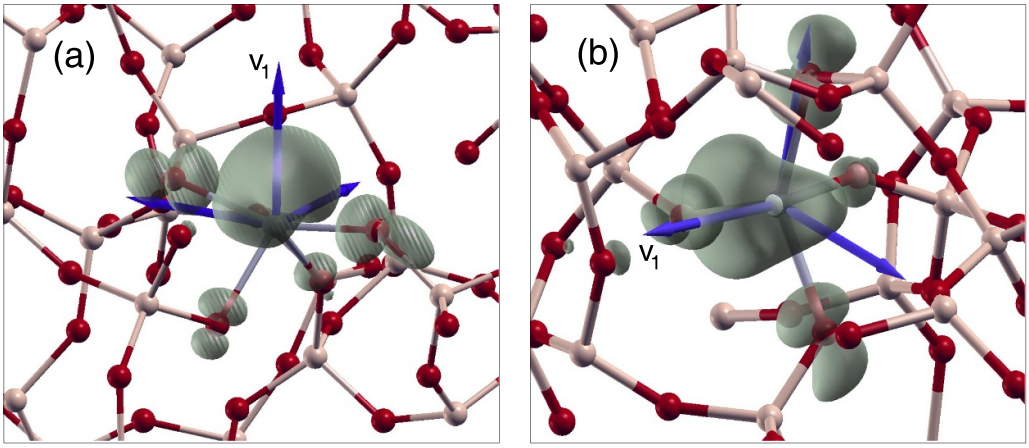

Figure 3. Spin densities (shadowed) and principal directions (blue arrows) of the g-tensor of (a) a tin STE configuration of the orthorhombic 'Griscom type'. The principal direction (v_1) relative to $g_1 \sim g_e$ is along the bisector of the wide O–Sn–O angle (159.7°), (b) a tin STE configuration of the "quasi-axial" kind featuring a widest O–Sn–O angle of 131.8°. The principal direction (v_1) relative to $g_1 \sim g_e$ is almost parallel to a Sn–O bond.

3.4. STE configurations at a fourfold coordinated Sn site: the Sn(1) center

In the tin STE configurations, figure 3, the SnO_4 tetrahedron is distorted from the ideal geometry (point group T_d) as consequence of the localization of an extra electron in close analogy with the electronic structure of the Ge(1) center in Ge-doped silica [33, 36]. The vast majority (∼80%) of the tin STE here calculated are markedly of the orthorhombic kind, hereafter also called 'Griscom' kind [75, 76], shown in figure 3(a). In the Griscom STE, following the capture of the electron at a SnO_4 tetrahedron, one O–Sn–O angle opens up (∼140−170°) with the two Sn–O bonds becoming slightly longer (∼2.1 Å) with respect to the usual bond length in Sn-E' (∼2 Å). In figure 3(b) we show the structure and spin density of another kind of geometry for the tin STE configuration. The SnO_4 tetrahedron is also quite strained, resembling a pyramid, with oxygen atoms at vertexes and the Sn atom at the center of the basis (i.e. lying on the O–O–O plane, with O–Sn–O angles smaller than 140°), and with the spin-density of the unpaired electron localized around the Sn atom, on the basis (O–O–O) of the pyramid.

In table 2 we give the average g-values and $A_{iso}(^{119}Sn)$ Fermi contact calculated for the STE configurations in our Sn-doped silica models (figure 4). As seen for the Sn-E' and Sn–FO, the absolute values of $A_{iso}(^{119}Sn)$ calculated for the tin STE configurations are huge, on average ∼490 mT, about 20% larger than those calculated for the Sn-E' configurations. Such a relative difference corresponds to the relative difference between the Fermi contacts of Ge(1) and Ge-E' centers [33]. Dipolar (anisotropic terms) calculated for the tin STE configurations are even smaller ($|\boldsymbol{A}_{dip}|/A_{iso}$ ∼1.3%) that those found for the Sn-E' centers. This is very close to the weight of dipolar terms as calculated for the Ge(1) center in silica (∼2%) [33, 69]. The A_{iso} values given in table 2 indicate a strong component of the Sn 5s orbital in the unpaired electron wave function. In terms of total wave function, the contribution of the 5s orbital (based on the formula $C_s^2 = A_{iso}/A_s$ where A_s refers to the free atomic value [77]) is around ∼30%–40% [11, 31] for the tin STE, to be compared with the estimate of 35% of Watanabe *et al* [77] given for the Ge center.

Figure 4(b) shows the existence of a trend between the A_{iso}(Sn) and the g_{13} values in the STE configurations. Such a trend is related to a structural variation of the SnO_4 tetrahedron, in analogy with what was previously remarked in Ge-doped silica [33]. In fact, in figures 5(a) and (b) we show the existence of a dependence of the g_{12}, g_{13} and A_{iso}(Sn) values on the widening of an O–Sn–O angle of the tin STE (figure 3(a)). Figures 5(a) and (b) confirm and generalize the analogous relation described for the Ge(1) centers in [33] but based on a very small number of configurations. For O–Sn–O angles smaller than 140°, one can find several STE configurations that can be classified as quasi-axial or nearly axial as shown in figure 3(b). Quasi-axial STE configurations tend to show larger A_{iso} and also larger g_1 values (by ∼1000 ppm) than Griscom's STE. On average quasi-axial tin STE feature the following g-tensor principal values $g_1 = 2.0035$, $g_2 = 1.9936$ and $g_3 = 1.9881$.

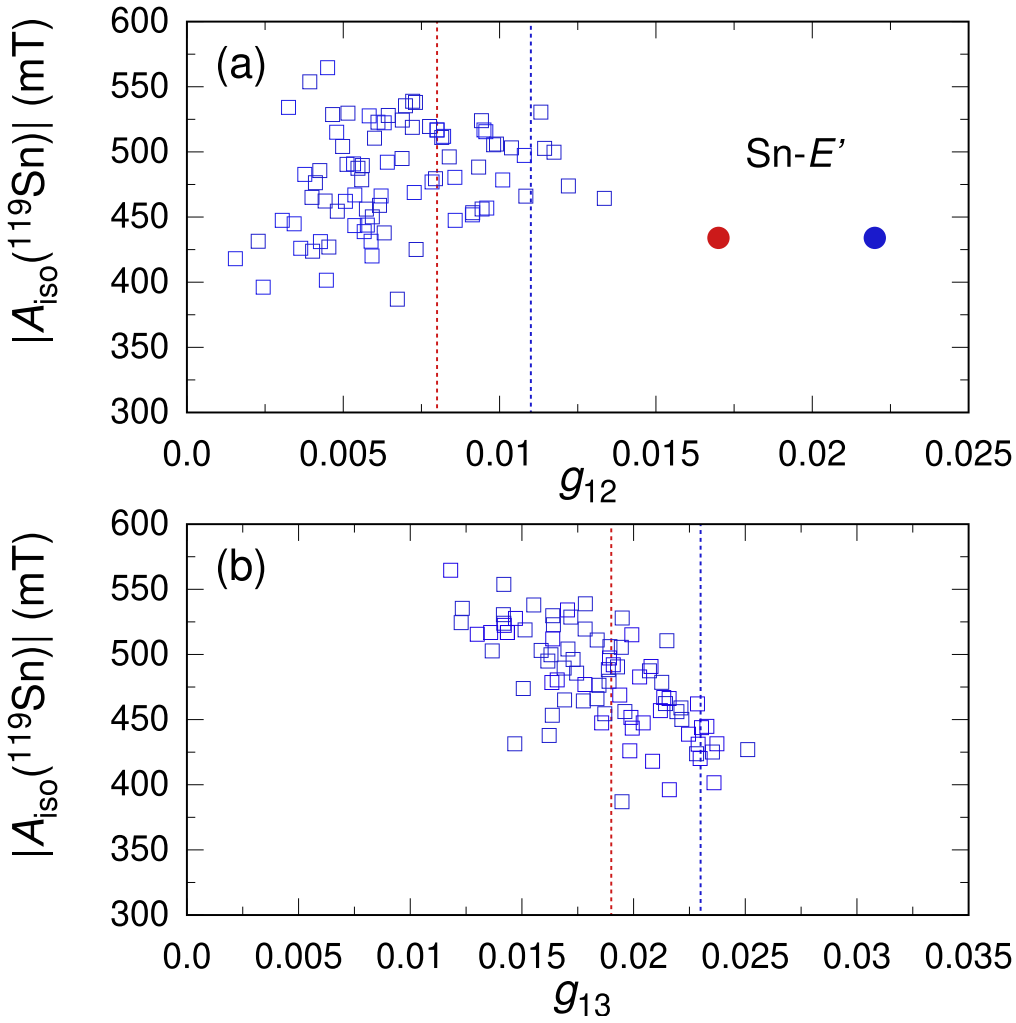

Figure 4. $|A_{iso}(^{119}Sn)|$ vs g_{12} and g_{13}, as here calculated by first-principles for tin STE configurations in model I and model II (blue squares). Experimental data of the axial Sn-E' (red [11] and blue [37] discs) and orthorhombic EPR signals (red [11] and blue [37] vertical lines) are shown.

4. Discussion

In Ge-doped silica the Ge(1) and Ge-E' centers are universally attributed to an electron localized at a four-fold Ge atom and to a Ge paramagnetic defect analogous to the E'_γ in SiO_2, respectively [33, 75, 78]. The origin of the Ge(2) defect, detected in both Ge-doped SiO_2 [22, 71, 79–83], and high purity *v*-GeO_2 [84], has been very controversial for long time and only recently clarified thanks to first principles calculations [33]. In the present paper, by exploiting the paramagnetic centers configurations generated in the adopted model I and II of *v*-SiO_2 [33, 58], we show that the EPR signals due to Sn paramagnetic defects discussed in [11, 37] have to be ascribed to two different kinds of Sn point defects. A first kind, corresponding to the axial EPR signal in [11, 37], has to be attributed to a defect analogous to the E'_γ in SiO_2 i.e. a Sn-E' center which is a hole trap (figure 1(a)). A second kind, responsible for the orthorhombic EPR signal in [11, 37], has to be attributed to a point defect, analogous to the Ge(1) center, consisting in an electron trapped at a SnO_4 tetrahedron i.e. a Sn(1) center (figure 3). We note that such an electron center, the Sn(1) center, provides a more likely explanation for the absorption bands at ∼4.4 and ∼5.4 eV than the model put forward by [15], i.e. the $(Sn^{4+})^-$ center, which requires a six-fold coordination for the tin atom that is never realized in our calculations and seems very unlikely for low tin concentration in silica. The considerable disorder broadening in figure 3(c) of [11] was regarded as attributable to the expected occurrence of a subset of low-symmetry Sn-E' variants arising from Sn sites coordinated through bridging oxygen atoms bound to three unequivalent atoms, in particular to combinations such as two Si and one Sn, or one Si and two Sn. We note that the former would involve two close Sn atoms (the central one hosting the unpaired spin) and the latter a cluster with three nearby Sn atoms, which for low Sn concentrations might be very questionable. Moreover, by direct testing (table 3) we could rule out the relevance of these configurations as far as concerns the orthorhombic EPR signal of [11, 37]. The Sn(1) center add upon the known series of electron centers trapped at a tetrahedral impurity in silica, together e.g. with the P_2 and the Ge(1) centers [33, 76, 85]. The existence of another similar electron center, that we here label as the Si(1) center,

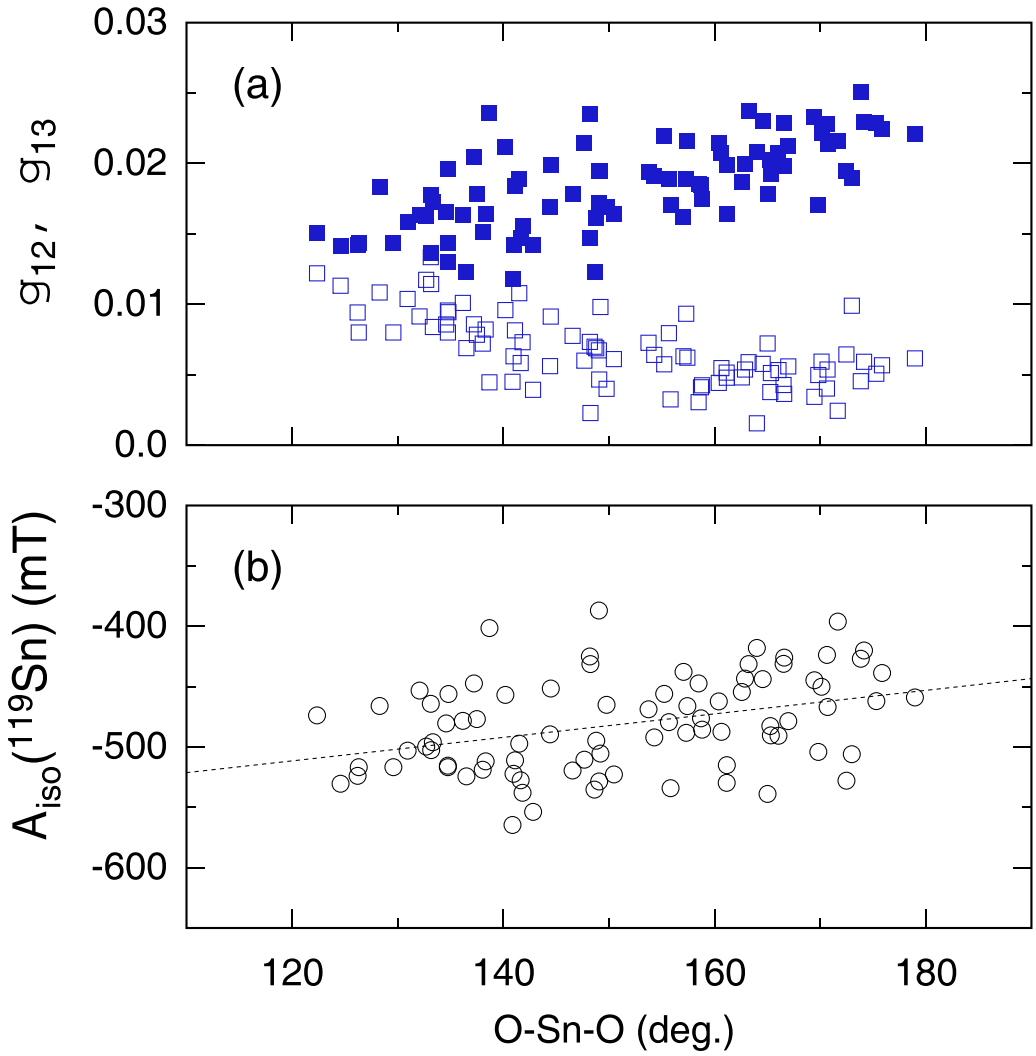

Figure 5. Calculated (a) g_{12} (empty squares) g_{13} (filled squares) values, and (b) Fermi contact $A_{iso}(^{119}Sn)$ plotted vs widest O–Sn–O angle of the Sn tetrahedron in the tin STE configurations of model I and model II.

was put forward based on theoretical calculations by El-Sayed *et al* [78], but has not yet been confirmed by experimental EPR investigations.

As far as concerns the result of [11, 24, 37] we also suggest that the analogy between Sn-doped silica and Ge-doped silica can be pushed further, and that a Sn(2) center may exist (figure 1(b)), though less abundant than the Sn(1) and Sn-E' centers, and be the tin analogous of the Ge(2) and E'_α centers. From an experimental point of view, the EPR spectrum of the Sn(2) center could be obtained after the subtraction of an appropriate fraction of the Sn(1) and Sn-E' signals similarly to the procedure usually adopted for obtaining the Ge(2) spectrum. The width of the EPR signal provides the relative difference $g_{13} = g_1 - g_3$ between g_1, g_3 values:

$$g_{13} = \frac{h\nu}{H_1\beta} - \frac{h\nu}{H_3\beta} \qquad (1)$$

where β is the Bohr magneton, H_1 and H_3 are the field positions of the main positive peak and of the farthest negative peak, respectively. Hence, the g_{13} value can be known with a very good accuracy as it corresponds to the whole width of the Ge(2), or Sn(2), EPR signal and is not biased by offset errors that could affect the experimental estimate of the g principal values. At variance, the $g_{12} = g_1 - g_2$ value is obtained by finding the first zero crossing value on the high field side of the main peak [76, 83]. This procedure however can lead to a considerable position error in g_2 values seen in experiments [83, 86].

From Chiodini's data of [37], by using the equation (1), and by assuming that the small dimple located at ∼350 mT in figure 2 of [37] is a fingerprint of the Sn(2) center, we estimate, with $\nu = 9.6$ GHz, a g_{13} value of ∼0.0360 that is within one std from the average g_{13} value (0.0394) given in table 2 for the Sn–FO configurations. We note that in [33] the calculated g_{13} of Ge–FO configurations coincides with the experimental g_{13} values of the Ge(2) center and are clearly larger (double) than g_{13} values of other centers like Ge-E' and Ge(1) centers. Hence, we infer that the calculated g_{13} values obtained in this work for Sn–FO should be very close to those that one could extract from the experimental spectra for the here identified Sn(2) center.

Table 4. Isoelectronic series (X = Si, Ge, Sn) of several point defects in silica as nowadays known from the present investigation and from [11, 17, 33, 35, 58, 78, 88]. The dotted $\dot{X}$ is used to indicate the atom hosting the unpaired electron. Dashes − and—indicate the bond with a bridging oxygen atom and with a threefold-coordinated oxygen atom, respectively. The * indicates still under debate, not yet observed with EPR.

X	$\equiv\dot{X}$	$=\dot{X}$—	$(\dot{X}O_4)$	$-X-$	$=\dot{X}$–H
Si	E'_γ	E'_α	Si(1)*	twofold Si	H(I)
Ge	Ge-E'	Ge(2)	Ge(1)	twofold Ge	H(II)
Sn	Sn-E'	Sn(2)	Sn(1)	twofold Sn	H(III)

Moreover, Δg values for E'-like centers in silica are, within first-order perturbative approximation [72, 87], proportional to the spin–orbit coupling constant λ. Thus we may infer that a Sn(2) center should possess a $g_{13}^{Sn(2)} = (\lambda_{Sn}/\lambda_{Ge})g_{13}^{Ge(2)}$ and also that [11, 33]:

$$\frac{\lambda_{Sn}}{\lambda_{Ge}} = \frac{g_{13}^{Sn-E'}}{g_{13}^{Ge-E'}} \sim 0.0170/0.007 = 2.43. \quad (2)$$

Keeping into account that for Ge(2) the g_{13} is 0.001 43 [71], we may roughly estimate for the Sn(2) center:

$$g_{13}^{Sn(2)} = \left(\frac{\lambda_{Sn}}{\lambda_{Ge}}\right) g_{13}^{Ge(2)} = 2.43 \cdot 0.001\,43 \sim 0.0350. \quad (3)$$

This value is quite close to the g_{13} values as calculated from first-principles for the Sn–FO configurations (table 2) and also as estimated here above using equation (1). The larger spin–orbit coupling of Sn with respect to Ge also supports a non zero value for the $g_{23} = g_2 - g_3$ difference in Sn-E' centers. In fact, for Ge-E' centers an experimental estimate [71] of $g_{23} = 0.0010$ was given, and by following similar reasonings as here above one could then estimate for Sn-E' centers a $g_{23} \sim 0.0025$, which is not so far from the experimental $g_{23} = 0.0042$ of [24]. Moreover our calculations (table 2) further support a slightly orthorhombic (nearly axial) g-tensor for the Sn-E' centers rather than an ideal axial symmetry as it was assumed in [11].

Concerning the (neutral) defect precursors of Sn-E' centers, Hayakawa *et al* [24] suggested that a conversion of twofold Sn centers to Sn-E' centers could take place in x−ray irradiated $5SnO_2$-$95SiO_2$ glass. Hayakawa *et al* [24] also supposes that the conversion from twofold Sn centers to Sn-E' centers should be similar to the one observed in irradiated Ge-doped SiO_2 glass where the optical absorption due to the twofold Ge, i.e. the germanium lone pair centers (GLPC), is bleached under irradiation with concomitant generation of Ge(1), Ge-E' and Ge(2) centers [22, 33]. The present investigation further supports the radiation induced generation mechanisms proposed by [24], since a strict analogy exists in silica between the family of Ge paramagnetic and Sn paramagnetic centers (table 4). The Sn–FO, in analogy to Si–FO and Ge–FO configurations, should be generated by the ionization of a twofold coordinated Sn atom and subsequent relaxation of the defect structure [33, 58]. It is however quite likely that the relative concentration ratios of Sn(1), Sn-E' and Sn(2) centers will differ with respect to those observed for Ge centers. However a precise evaluation of these ratios is beyond the scope of the present paper.

5. Conclusion

In conclusion, our study, by analyzing the EPR parameters distributions of a large amount of defect configurations, provides evidence for an assignment of the orthorhombic EPR signal found by Chiodini *et al* [11] to a Sn(1) center, structurally analogous to the Ge(1) center [33], consisting in an unpaired electron trapped at a distorted SnO_4 tetrahedron. Furthermore, we argue that a Sn(2) center arising from Sn–FO configurations should also appear in the EPR spectra, and in particular we suggest its presence in the EPR spectra of [37]. More specifically, the Sn(2) center arises from an unpaired spin localized at a three-fold Sn atom which is bonded to a three-fold oxygen atom through a weak Sn–O bond, ∼0.3 Å longer than usual Sn–O bonds of Sn-E' centers in Sn-doped silica.

The successful identification, by means of first-principle calculations of EPR parameters, of the two Sn paramagnetic defects in Sn-doped silica, the Sn(1) and Sn(2) centers, allows us to infer that an extended analogy exists between the family of Ge paramagnetic defects and the one of Sn paramagnetic defects for low Sn doping content. Moreover the larger number of Sn(1) configurations here analyzed with respect to the Ge(1) configurations of [33] allows us to infer a better description also of the electronic structure of the Ge(1) center which, similarly to the Sn(1) center, should arise mainly from markedly orthorhombic tin STE configurations (figure 3(a)).

Yet, given the higher ionicity of Sn–O bond with respect of the Ge–O bond, and given the likely smaller energy barriers for defect diffusion and interconversion in Sn-doped silica with respect to Ge-doped silica, the thermal and aging behavior of the Sn(1) and Sn(2) centers may differ substantially from the one observed for the analogous Ge-related centers. We hope that the latter issue and as well as the optical activity (absorption/emission...) of the Sn-related defects will be matter of future investigations which will be necessary for a complete overview/understanding of Sn point defects in silica, and that eventually will support a wider usage of Sn-doped silica for applications in fiber-optics and microelectronics.

Data availability statement

All data that support the findings of this study are included within the article (and any supplementary files).

Acknowledgments

We acknowledge Prof. S Girard for useful discussions and suggestions. We also acknowledge Prof. U Gerstmann for sharing the tin pseudopotential file of [52] that we employed for benchmarks with the converse code [53]. The calculations in this work were performed using the HPC resources of CINECA (Projects ISCRA-C HP10C75EVG 'FirESS' and HP10C2GG7R 'NFFAM').

Conflict of interest

There are no conflicts to declare.

ORCID iDs

L Giacomazzi https://orcid.org/0000-0003-2499-4276
D Ceresoli https://orcid.org/0000-0002-9831-0773

References

[1] Fitting H J 2009 *J. Lumin.* **129** 1488–92
[2] Zatsepin D, Zatsepin A, Boukhvalov D, Kurmaev E and Gavrilov N 2016 *Appl. Surf. Sci.* **367** 320–6
[3] Romanov I, Komarov F, Milchanin O, Vlasukova L, Parkhomenko I, Makhavikou M, Wendler E, Mudryi A and Togambayeva A 2019 *J. Nanomater.* **2019** 9486745
[4] Romanov I, Komarov F, Parkhomenko I, Vlasukova L, Makhavikou M, Milchanin O, Wendler E, van Vuuren A and Neethling J 2022 *Mater. Lett.* **308** 131070
[5] Shiratori D, Kimura H, Nakauchi D, Kato T, Kawaguchi N and Yanagida T 2020 *Radiat. Meas.* **134** 106297
[6] Chiodini N, Paleari A and Spinolo G 2003 *Phys. Rev. Lett.* **90** 055507
[7] Tran T N L *et al* 2020 *Opt. Mater.* X **7** 100056
[8] Lam Tran T N, Szczurek A, Carlotto A, Varas S, Righini G C, Ferrari M, Krzak J, Lukowiak A and Chiasera A 2022 *Opt. Mater.* **130** 112577
[9] Brambilla G, Pruneri V and Reekie L 2000 *Appl. Phys. Lett.* **76** 807–9
[10] Brambilla G and Pruneri V 2001 *IEEE J. Sel. Top. Quantum Electron.* **7** 403–8
[11] Chiodini N, Meinardi F, Morazzoni F, Paleari A, Scotti R and Spinolo G 1998 *Phys. Rev.* B **58** 9615–8
[12] Chiodini N, Ghidini S, Paleari A, Brambilla G and Pruneri V 2000 *Appl. Phys. Lett.* **77** 3701–3
[13] Paleari A, Meinardi F, Brovelli S and Lorenzi R 2018 *Commun. Phys.* **1** 67
[14] Rybaltovskii A, Kamenskikh I, Mikhailin V, Semenova N, Spasskii D, Zimmerer G, Chernov P and Golant K 2002 *Glass Phys. Chem.* **28** 379–88
[15] Nakanishi T, Fujimaki M, Tokuhiro S i, Nomura K I, Ohki Y and Imamura K 2003 *J. Non-Cryst. Solids* **318** 87–94
[16] Chiodini N, Meinardi F, Morazzoni F, Padovani J, Paleari A, Scotti R and Spinolo G 2001 *J. Mater. Chem.* **11** 926–9
[17] Skuja L 1992 *J. Non-Cryst. Solids* **149** 77–95
[18] D'Amico M, Messina F, Cannas M, Leone M and Boscaino R 2008 *J. Phys. Chem.* A **112** 12104–8
[19] Paleari A, Brovelli S, Meinardi F, Lorenzi R, Lauria A, Mochenova N, Vodopivec B and Chiodini N 2009 *J. Non-Cryst. Solids* **355** 1024–7
[20] Richard N, Martin-Samos L, Girard S, Ruini A, Boukenter A, Ouerdane Y and Meunier J 2013 *J. Phys.: Condens. Matter* **25** 335502
[21] Trukhin A, Golant K and Teteris J 2013 *J. Non-Cryst. Solids* **367** 53–57
[22] Fujimaki M, Watanabe T, Katoh T, Kasahara T, Miyazaki N, Ohki Y and Nishikawa H 1998 *Phys. Rev.* B **57** 3920–6
[23] Yang K, Zheng S, Jiang X, Fan S and Chen D 2017 *Mater. Lett.* **204** 5–7
[24] Hayakawa T, Enomoto T and Nogami M 2006 *Jpn. J. Appl. Phys.* **45** 5078
[25] Jiménez J A, Crawford C L and Lascola R J 2022 *J. Am. Ceram. Soc.* **105** 4009–26
[26] Kweon K E and Lordi V 2018 *J. Non-Cryst. Solids* **492** 108–14
[27] Masai H, Fujiwara T, Matsumoto S, Tokuda Y and Yoko T 2014 *J. Non-Cryst. Solids* **383** 184–7
[28] Liu Z, Chen H, Huang W, Gu J, Bu W, Hua Z and Shi J 2006 *J. Mater. Res.* **21** 655–63
[29] Brunthaler G, Jantsch W, Kaufmann U and Schneider J 1985 *Phys. Rev.* B **31** 1239–43
[30] Girard S *et al* 2019 *Rev. Phys.* **4** 100032
[31] Kawazoe H, Nishii J, Hosono H, Kanazawa T and Imagawa H 1982 *Le J. Phys. Colloques* **43** C9–155
[32] Pickard C J and Mauri F 2002 *Phys. Rev. Lett.* **88** 086403
[33] Giacomazzi L, Martin-Samos L, Boukenter A, Ouerdane Y, Girard S and Richard N 2015 *Opt. Mater. Express* **5** 1054–64
[34] Giacomazzi L, Martin-Samos L, Boukenter A, Ouerdane Y, Girard S, Alessi A, de Gironcoli S and Richard N 2017 *Nanotechnology* **28** 195202
[35] Pacchioni G and Ferrario R 1998 *Phys. Rev.* B **58** 6090
[36] Du J, René Corrales L, Tsemekhman K and Bylaska E J 2007 *Nucl. Instrum. Methods Phys. Res.* B **255** 188–94
[37] Chiodini N, Ghidini S and Paleari A 2001 *Phys. Rev.* B **64** 073102
[38] Chiodini N, Meinardi F, Morazzoni F, Paleari A, Scotti R and Spinolo G 1998 *MRS Online Proc. Libr.* **540** 383–8
[39] Perdew J P, Burke K and Ernzerhof M 1996 *Phys. Rev. Lett.* **77** 3865
[40] Tantardini C, Kvashnin A G and Ceresoli D 2022 *Materials* **15** 3347
[41] Ceresoli D 2024 Si, O, Sn pseudopotentials (available at: https://sites.google.com/site/dceresoli/pseudopotentials) (Accessed 30 January 2024)
[42] Szymanski M A, Shluger A L and Stoneham A M 2001 *Phys. Rev.* B **63** 224207
[43] Giannozzi P *et al* 2009 *J. Phys.: Condens. Matter* **21** 395502
[44] Giannozzi P *et al* 2020 *J. Chem. Phys.* **152** 154105
[45] Gerstmann U 2011 *Phys. Status Solidi* b **248** 1319–36
[46] Blügel S, Akai H, Zeller R and Dederichs P 1987 *Phys. Rev.* B **35** 3271
[47] Blöchl P E 2000 *Phys. Rev.* B **62** 6158–79
[48] Stone N 2005 *At. Data Nucl. Data Tables* **90** 75–176
[49] Schreckenbach G and Ziegler T 1997 *J. Phys. Chem.* A **101** 3388–99
[50] Declerck R, Van Speybroeck V and Waroquier M 2006 *Phys. Rev.* B **73** 115113
[51] Gerstmann U, Seitsonen A P, Ceresoli D, Mauri F, von Bardeleben H J, Cantin J L and Garcia Lopez J 2010 *Phys. Rev.* B **81** 195208
[52] Ceresoli D, Gerstmann U, Seitsonen A P and Mauri F 2010 *Phys. Rev.* B **81** 060409
[53] Ceresoli D A converse-NMR method for Quantum-Espresso (available at: https://code.google.com/archive/p/converse-nmr/) (Accessed 30 January 2024)
[54] Van Yperen-De Deyne A, Pauwels E, Van Speybroeck V and Waroquier M 2012 *Phys. Chem. Chem. Phys.* **14** 10690–704
[55] Komorovský S, Repiský M, Malkina O L, Malkin V G, Malkin I and Kaupp M 2006 *J. Chem. Phys.* **124** 084108

[56] Belanzoni P, van Lenthe E and Baerends E J 2001 *J. Chem. Phys.* **114** 4421–33
[57] Richard N, Martin-Samos L, Roma G, Limoge Y and Crocombette J P 2005 *J. Non-Cryst. Solids* **351** 1825–9
[58] Giacomazzi L, Martin-Samos L, Boukenter A, Ouerdane Y, Girard S and Richard N 2014 *Phys. Rev.* B **90** 014108
[59] Martin-Samos L, Limoge Y, Crocombette J P, Roma G, Richard N, Anglada E and Artacho E 2005 *Phys. Rev.* B **71** 014116
[60] Giacomazzi L, Umari P and Pasquarello A 2009 *Phys. Rev.* B **79** 064202
[61] Giacomazzi L, Umari P and Pasquarello A 2019 Medium-range structure of vitreous SiO2 *Materials Cloud Archive* 2019.0086/v1 (available at: https://archive.materialscloud.org/record/2019.0086/v1)
[62] Giacomazzi L 2024 Configurations of paramagnetic point defects in tin doped silica glass *Zenodo* (https://doi.org/10.5281/zenodo.10566923)
[63] Skuja L 1998 *J. Non-Cryst. Solids* **239** 16–48
[64] Lehnig M, Apoussidid T and Neumann W 1983 *Chem. Phys. Lett.* **100** 189–92
[65] Kurzbach D, Yao S, Hinderberger D and Klinkhammer K W 2010 *Dalton Trans.* **39** 6449–59
[66] The Materials Project 2020 Materials data on SnO_2 by materials project (available at: https://doi.org/10.17188/1272823)
[67] Sinha A K, Manna P K, Pradhan M, Mondal C, Yusuf S M and Pal T 2014 *RSC Adv.* **4** 208–11
[68] Uchino T and Yoko T 2006 *Phys. Rev.* B **74** 125203
[69] Pacchioni G and Mazzeo C 2000 *Phys. Rev.* B **62** 5452–60
[70] Kokalj A 1999 *J. Mol. Graph. Model.* **17** 176–9
[71] Agnello S, Alessi A, Gelardi F, Boscaino R, Parlato A, Grandi S and Magistris A 2008 *Eur. Phys. J.* B **61** 25–31
[72] Feigl F and Anderson J 1970 *J. Phys. Chem. Solids* **31** 575–96
[73] von Bardeleben H J, Cantin J L, Vrielinck H, Callens F, Binet L, Rauls E and Gerstmann U 2014 *Phys. Rev.* B **90** 085203
[74] Pietrucci F, Bernasconi M, Di Valentin C, Mauri F and Pickard C J 2006 *Phys. Rev.* B **73** 134112
[75] Griscom D L 2011 *J. Non-Cryst. Solids* **357** 1945–62
[76] Friebele E, Griscom D and Sigel J G 1974 *J. Appl. Phys.* **45** 3424–8
[77] Watanabe Y, Kawazoe H, Shibuya K and Ken-ichi M 1986 *Jpn. J. Appl. Phys.* **25** 425
[78] El-Sayed A M, Watkins M B, Afanas'ev V V and Shluger A L 2014 *Phys. Rev.* B **89** 125201
[79] Nishii J, Fukumi K, Yamanaka H, Kawamura K i, Hosono H and Kawazoe H 1995 *Phys. Rev.* B **52** 1661
[80] Fujimaki M, Kasahara T, Shimoto S, Miyazaki N, Tokuhiro S I, Soo Seol K and Ohki Y 1999 *Phys. Rev.* B **60** 4682–7
[81] Chiodini N, Meinardi F, Morazzoni F, Paleari A and Scotti R 1999 *Phys. Rev.* B **60** 2429–35
[82] Yamaguchi M, Saito K and Ikushima A J 2002 *Phys. Rev.* B **66** 132106
[83] Alessi A, Agnello S, Gelardi F, Messina G and Carpanese M 2011 *J. Non-Cryst. Solids* **357** 1900–3
[84] Tsai T, Griscom D L, Friebele E J and Fleming J W 1987 *J. Appl. Phys.* **62** 2264–8
[85] Pacchioni G, Erbetta D, Ricci D and Fanciulli M 2001 *J. Phys. Chem.* B **105** 6097–102
[86] Griscom D L 1990 Electron spin resonance *Glass Science and Technology: Advances In Structural Analysis* vol 4B, ed D R Uhlmann and N J Kreidl (Academic)
[87] Griscom D L 1984 *Nucl. Instrum. Methods Phys. Res.* B **1** 481–8
[88] Griscom D L 1991 *J. Ceram. Soc. Japan* **99** 923–42